

LARGE EDDY SIMULATION OF SELF-EXCITED ACOUSTIC OSCILLATIONS IN A THERMOACOUSTIC ENGINE

Geng Chen¹, Yufan Wang², Lihua Tang^{1*}, Kai Wang³, Brian R Mace¹

1 Department of Mechanical Engineering, University of Auckland, 20 Symonds Street, Auckland 1010, New Zealand

2 The State Key Laboratory of Fluid Power and Mechatronic Systems, Zhejiang University, Hangzhou 310027, China

3 Department of Chemical Engineering, Imperial College London, London, SW7 2AZ, United Kingdom

ABSTRACT

In this paper, we present three-dimensional (3-D) large eddy simulations (LES) of the thermally-induced oscillatory flow inside a full-scale quarter-wavelength standing-wave thermoacoustic engine (TAE). The TAE comprises a hot buffer, a stack and a resonator. Compressible nonlinear governing equations together with the equation of state are solved by the computational fluid dynamic (CFD) solver with the optimal node number and time step size. Numerical results show that self-excited acoustic oscillations occur inside the TAE, undergoing exponential growth, saturation and limit-cycle processes. It is also found that fundamental-mode standing-waves dominate the limit-cycle acoustic oscillations while higher-order harmonics coexist. The velocity profiles in the radial direction are highly affected by the Stokes number, displaying Poiseuille flow patterns in the stack channels and Richardson's annular effects in the resonator. The vortex shedding at the stack ends contributes to kinetic energy and heat losses as presented by the three-dimensional vorticity and time-averaged mass flux contours. The developed 3-D LES framework in this study provides high-fidelity simulations of thermoacoustic oscillations, deepening the understanding of multi-dimensional thermoacoustic effect and various nonlinear phenomena in the large-amplitude regime.

Keywords: thermoacoustic engine, large eddy simulation, self-excited acoustic oscillations, vortex shedding.

1. INTRODUCTION

Thermoacoustic engines (TAEs) are heat engines capable of converting external heat into useful acoustic energy. The acoustic energy could be subsequently converted into electricity using acoustic-to-electric transducers such as linear alternators [1], piezoelectric transducers [2], etc. The underlying mechanism behind the TAEs is the thermoacoustic effect which concerns the interactions between oscillatory flow and heat release at the fluid/solid interfaces. An excellent review paper on the design and fabrication of TAEs was given by Swift [3].

Linear thermoacoustic theory has difficulty in predicting the limit-cycle behaviors if the TAE is affected by nonlinearity in the large-amplitude regime. Besides, the transient performance cannot be examined by the quasi-one-dimensional frequency-domain codes based on the linear theory. Hence, computational fluid dynamic (CFD) techniques are commonly utilized to investigate the self-excited, large-amplitude thermoacoustic oscillations in the time domain. Previous reports on the CFD simulation of TAEs can be found in the literature [4-7]. However, the main challenge of CFD simulation is that it is often time-consuming and computationally expensive, especially for simulating full-scale thermoacoustic devices in which multiple scales of time and space are involved. Previous researchers normally conducted simulations based on a two-dimensional (2-D) subdomain of a full-scale TAE [8], which limits the applicability of advanced CFD methods.

In this paper, we carry out large eddy simulations (LES) of a full-scale three-dimensional (3-D) quarter-

wavelength standing-wave thermoacoustic engine. High performance computing (HPC) is employed to carry out such simulations. The numerical methods applied in this study are briefly introduced in Section 2. Simulation results and discussion are presented in Section 3. Finally, concluding remarks are drawn in Section 4.

2. NUMERICAL SIMULATION

Figure 1 depicts the three-dimensional (3-D) computational model of a quarter-wavelength standing-wave thermoacoustic engine (TAE) in this study. The TAE, comprised of a hot buffer, a stack and a resonator, is closed by a rigid wall at the left end and open at the other end. Air at atmospheric pressure is chosen as the working fluid. For brevity, a linear temperature distribution (from $T_h=700$ K to $T_c=300$ K) is enforced on the surfaces of the stack plates in place of the hot and cold heat exchangers, which provides the heating source to initiate thermoacoustic oscillations. As shown in Figure 1, the 3-D model is meshed with high-resolution structured grids. Exponential bunching laws are applied for the wall-surface and near-wall grids in order to save computational cost and capture the thermoacoustic effect which normally occurs within penetration depths from the wall surfaces.

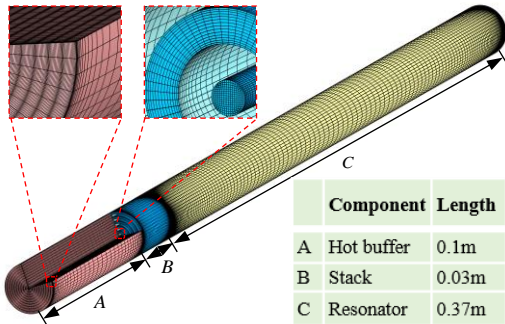


Fig 1 Computational model and mesh configurations of a quarter-wavelength standing-wave TAE. The TAE is composed of a hot buffer, a stack and a resonator, the dimensions of which are shown in the table

Three-dimensional nonlinear compressible governing equations together with state equation for an ideal gas are solved by the computational fluid dynamic (CFD) solver Fluent 18.1 on the structured grids. These equations are given as

$$\frac{\partial \rho}{\partial t} + \frac{\partial(\rho u_i)}{\partial x_i} = 0 \quad (1)$$

$$\frac{\partial(\rho u_i)}{\partial t} + \frac{\partial(\rho u_i u_j)}{\partial x_j} = -\frac{\partial p}{\partial x_i} + \frac{\partial \tau_{ij}}{\partial x_j} \quad (2)$$

$$c_p \frac{\partial(\rho T)}{\partial t} + c_p \frac{\partial(\rho u_i T)}{\partial x_i} = \frac{\partial}{\partial x_i} \left(\kappa \frac{\partial T}{\partial x_i} \right) + \tau_{ij} \frac{\partial u_j}{\partial x_i} + \frac{1}{\rho} \frac{\partial(\rho p)}{\partial t} + \frac{1}{\rho} \frac{\partial(\rho p u_i)}{\partial x_i} \quad (3)$$

$$p = \rho R g T \quad (4)$$

where the subscripts i and j are indices of the coordinates, κ is the thermal conductivity of the fluid, and τ_{ij} is the viscous stress tensor described by

$$\tau_{ij} = \mu \left(\frac{\partial u_i}{\partial x_j} + \frac{\partial u_j}{\partial x_i} \right) - \frac{2}{3} \mu \frac{\partial u_j}{\partial x_j} \delta_{ij} \quad (5)$$

where μ is the dynamic viscosity and δ_{ij} is the Kronecker delta. Non-slip conditions are enforced at all solid walls. Detailed settings of the CFD solver can be found in the literature [4]. Sensitivity tests show that the optimal node number is 497,210, and the optimal time step size is 1×10^{-5} s. Large eddy simulation (LES) is used to account for the turbulence occurred in the large-amplitude regime. The near-wall grid spacings in this study produce wall distance y plus (y^+) values of around 0.5, which are sufficient for obtaining high-resolution data. The maximum Courant-Friedrichs-Lewy (CFL) [9] of 0.45 is achieved at the selected time step size, ensuring that all the small eddies can be resolved.

3. RESULTS AND DISCUSSION

3.1 Self-excited oscillations and limit cycles

The time-dependent evolution of the closed-end pressure and open-end velocity disturbances is first simulated and displayed in Figure 2. The thermoacoustic oscillations experience exponential growth, saturation and finally limit cycles. In the limit cycle stage, the oscillating pressure and velocity are nearly $\pi/2$ out of phase, as shown in Figure 2(c), which indicates that standing waves dominate the acoustic oscillations. For the large-amplitude, limit-cycle acoustic oscillations, the

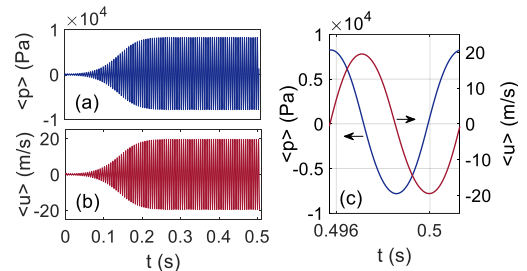


Fig 2 Time history of closed-end oscillating pressure and open-end oscillating velocity in the LES simulation at $T_h=700$ K: (a) closed-end pressure; (b) open-end velocity; (c) pressure and velocity in one acoustic cycle

maximum peak-to-peak pressure variation exceeds 16.3% of the ambient pressure and the local Mach number $M_0=|u|/c$ at the velocity antinode reaches 5.6%.

3.2 Excited unsteady oscillation modes

The oscillating pressure and velocity at different axial positions along the TAE can be decomposed into Fourier series, and are written as

$$\langle p \rangle = \langle p_0 \rangle + \sum_{n=1}^m \langle p_n \rangle \cos(\omega_n t) \quad (6)$$

$$\langle u \rangle = \langle u_0 \rangle + \sum_{n=1}^m \langle u_n \rangle \cos(\omega_n t + \theta_n) \quad (7)$$

where the mean value is denoted by subscript 0 and n stands for the n th harmonic of the fluctuations. θ is the phase between the pressure and velocity. It is found that the fundamental mode and higher-order harmonic oscillations coexist in the limit-cycle stage. Thus, the acoustic power is described by

$$I = \sum_{n=1}^m I_{2n} = \sum_{n=1}^m \frac{1}{2} A \langle p_n \rangle \langle u_n \rangle \cos \theta_n \quad (8)$$

Figure 3 shows the axial distributions of the acoustic pressure, velocity and acoustic power of the first two acoustic modes. \hat{p}_1 and \hat{u}_1 are the maximum pressure and velocity of the fundamental frequency. \hat{p}_2 and \hat{u}_2 are the maximum pressure and velocity of the second harmonic. The stack region, where the thermoacoustic energy conversion occurs, is shown as the shaded area. The acoustic power at the fundamental mode is much higher than the second harmonic. There is a power gain for the first-mode oscillations in the stack region while the acoustic power dissipates for the second-harmonic oscillations.

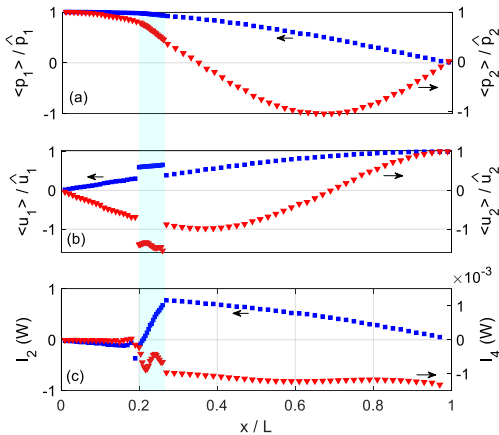


Fig 3 Excited acoustic oscillation modes at $T_h=700$ K from the LES simulation: (a) axial distributions of acoustic pressure, velocity and acoustic power for the fundamental mode; (b) axial distributions of acoustic pressure, velocity and acoustic power for the second harmonic

3.3 Near-wall velocity profiles

Swift [10] derived the analytical solution for the oscillating velocity from the linear momentum equation, which is

$$u = \begin{cases} \Re \left[\frac{P_A}{\omega} \left(1 - \frac{J_0 \left[\frac{(j-1)r}{\delta_v} \right]}{J_0 \left[\frac{(j-1)D}{2\delta_v} \right]} \right) e^{j\omega t} \right], & \text{circular tubes} \\ \Re \left[\frac{P_A}{\omega} \left(1 - \frac{\cosh \left(\frac{(1+j)y}{\delta_v} \right)}{\cosh \left(\frac{(1+j)d}{2\delta_v} \right)} \right) e^{j\omega t} \right], & \text{parallel plates} \end{cases} \quad (9)$$

where P_A is the pressure amplitude, $\Re[\]$ denotes the real part of a complex quantity, $\delta_v = \sqrt{2\nu/\omega}$ and $\delta_\alpha = \sqrt{2\alpha/\omega}$ denote the viscous and thermal penetration depths, respectively. J_n is the Bessel function of the first kind at n th order. $y=0$ corresponds to the centre of the parallel plates, and $r=0$ is the centre line of the tube. d is the plate gap and $D/2$ is the resonator radius as illustrated in Figure 4(a). The near-wall velocity profiles are characterized by the Stokes number,

$$S_t = \sqrt{\omega D_0^2 / \nu} = \sqrt{2} D_0 / \delta_v \quad (10)$$

where D_0 refers to the $d/2$ for the stack plates and $D/2$ for the resonator. Figure 4(b) plots the dimensionless velocity at different Stokes numbers ($S_t=1, 10$ and 30). When δ_v is large, e.g. in the stack channels, the entire flow is affected by viscosity and resembles a Poiseuille flow. When δ_v is small, e.g. in the resonator, only fluid close to the vicinity of the resonator wall is affected and exhibits Richardson's annular effects (overshoots) [11]. Our simulation results (not shown) are consistent with the theoretical analysis with $S_t=2.71$ in the stack channels and $S_t=88.97$ in the resonator. Similar patterns are also reported in previous numerical studies [6, 7].

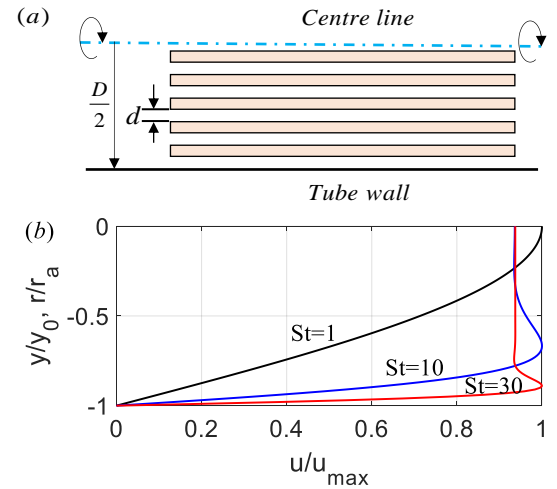


Fig 4 Instantaneous velocity profiles at the fluid/solid interfaces: (a) sketch of stack channels and resonator; (b) plot of theoretical estimations at $t=\pi/2\omega$

3.4 Vortex shedding

Vortex shedding happens at the stack ends where the cross-section of the oscillatory flow contracts or expands. Figure 5 illustrates the LES simulation of 3-D vortex core regions around the stack ends at eight consecutive instants in an acoustic cycle in the limit-cycle stage. The vorticity magnitude of the fluid is calculated by

$$|\boldsymbol{\omega}| = |\nabla \times \mathbf{u}| \quad (11)$$

where $\boldsymbol{\omega}$ is the vorticity and \mathbf{u} is the velocity vector. The method defining the vortex core region is Q-Criterion of level 0.01 in CFD-Post. At ϕ_1 and ϕ_4 , the space-averaged velocity in the middle of the stack is zero, and the strength of vortex at the ends of the stack is small. Toroidal vortex rings are observed at the stack left end, while broken rings and smaller eddies are found at the right end. At ϕ_3 and ϕ_7 , the velocities are maximum but in the opposite directions. The strength of the vortex rings also increases at these instants. The vortex core patterns are not symmetric at the stack ends due to the change of density/compressibility in the stack region where a temperature gradient is imposed. The breakdown of vortex rings at the stack ends indicates the loss of kinetic energy of the oscillatory flow. The 3-D representations of vortex shedding at the stack ends give insight into the underlying mechanism of minor losses in a thermoacoustic engine.

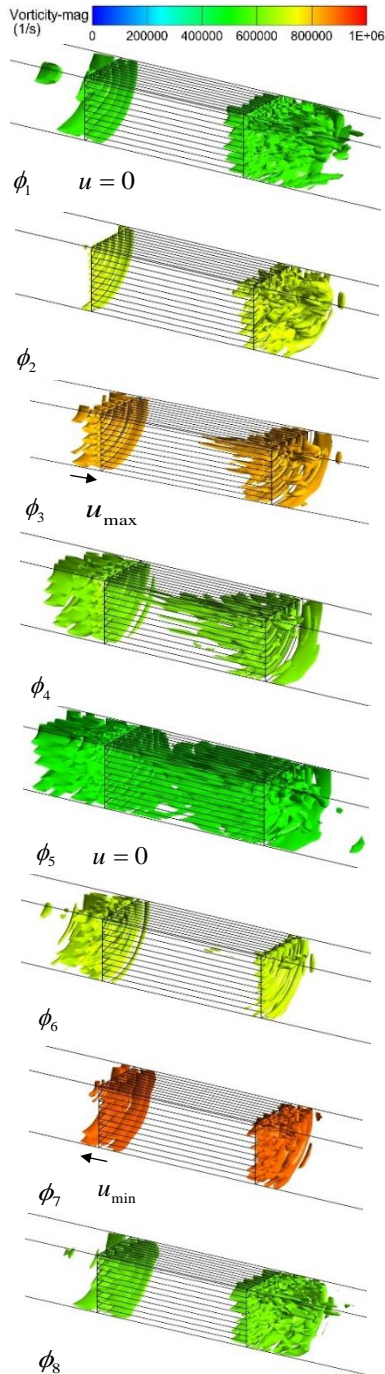


Fig 5 Contours of vortex shedding at the stack ends at eight different instants in an acoustic cycle at $T_h = 700$ K from the LES simulation

3.5 Jet-driven streaming

We observed the jet-driven mass streaming at the stack by plotting the time-averaged mass flux contours as shown in Figure 6. The non-zero mass fluxes at the stack ends arise from the vortex shedding process which forms small jets into the open space in the hot buffer/resonator. Consistent with the vortex core regions, the jet-driven streaming is most obvious at a short distance of the stack ends and weakens at the downstream of the jets. The jet-driven streaming is believed to contribute to undesirable heat losses through convective heat transportation [12].

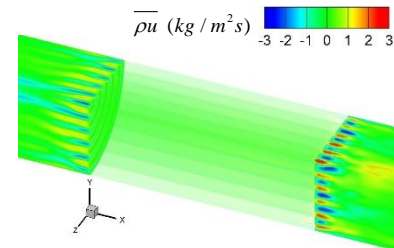


Fig 6 3-D time-averaged mass flux contour showing jet-driven streaming at the stack ends

4. CONCLUSIONS

Large eddy simulation (LES) of a quarter-wavelength standing-wave thermoacoustic engine (TAE) has been conducted in this study, in which large-amplitude self-excited thermoacoustic oscillations are observed. Decomposition of the oscillating pressure and velocity at different positions along the TAE shows that the fundamental mode standing waves dominate the

thermoacoustic oscillations. The Stokes number plays an important role in the velocity profiles in the stack channels as well as the resonator. The minor losses, caused by contraction and expansion of cross-section at the stack ends, are presented by 3-D representations of vortex core regions. The vortex shedding also gives rise to evident jet-driven mass streaming around the stack ends, which leads to undesirable heat losses. The numerical results shown in this work are useful for the design and optimization of efficient TAEs for practical industrial applications.

ACKNOWLEDGEMENT

High performance computing (HPC) provided by New Zealand eScience Infrastructure (NeSI) is acknowledged. The authors are grateful for the financial support from China Scholarship Council (no. 201608630046).

REFERENCE

- [1] Wang K, Sun D, Zhang J, Xu Y, Luo K, Zhang N, et al. An acoustically matched traveling-wave thermoacoustic generator achieving 750 W electric power. *Energy*. 2016;103:313-21.
- [2] Chen G, Tang L, Mace BR. Modelling and analysis of a thermoacoustic-piezoelectric energy harvester. *Applied Thermal Engineering*. 2019;150:532-44.
- [3] Swift GW. Thermoacoustic engines. *The Journal of the Acoustical Society of America*. 1988;84:1145-80.
- [4] Zink F, Viperman J, Schaefer L. CFD simulation of thermoacoustic cooling. *International journal of heat and mass transfer*. 2010;53:3940-6.
- [5] Scalo C, Lele SK, Hesselink L. Linear and nonlinear modelling of a theoretical travelling-wave thermoacoustic heat engine. *Journal of Fluid Mechanics*. 2015;766:368-404.
- [6] Kuzuu K, Hasegawa S. Numerical investigation of heated gas flow in a thermoacoustic device. *Applied Thermal Engineering*. 2017;110:1283-93.
- [7] El-Rahman AIA, Abdelfattah WA, Fouad MA. A 3D investigation of thermoacoustic fields in a square stack. *International Journal of Heat and Mass Transfer*. 2017;108:292-300.
- [8] Mergen S, Yıldırım E, Turkoglu H. Numerical study on effects of computational domain length on flow field in standing wave thermoacoustic couple. *Cryogenics*. 2019;98:139-47.
- [9] Anderson JD, Wendt J. *Computational fluid dynamics*: Springer; 1995.
- [10] Swift GW. *Thermoacoustics: A unifying perspective for some engines and refrigerators*: Springer; 2017.

[11] White FM, Corfield I. *Viscous fluid flow*: McGraw-Hill New York; 2006.

[12] Olson J, Swift G. Acoustic streaming in pulse tube refrigerators: tapered pulse tubes. *Cryogenics*. 1997;37:769-76.